Available online at www.sciencedirect.com
ScienceDirect
Journal of Computational Physics 227 (2008) 4142–4161
JOURNAL OF COMPUTATIONAL PHYSICS
www.elsevier.com/locate/jcp

Effects of direction decoupling in flux calculation in finite volume solvers

M.R. Smith [a,*], M.N. Macrossan [a], M.M. Abdel-jawad [b]

[a] *Centre for Hypersonics, The University of Queensland, Australia*
[b] *ARC Centre for Functional Nanomaterials, The University of Queensland, Brisbane 4072, Australia*

Received 4 May 2007; received in revised form 12 December 2007; accepted 18 December 2007
Available online 31 December 2007

Abstract

In a finite volume CFD method for unsteady flow fluxes of mass, momentum and energy are exchanged between cells over a series of small time steps. The conventional approach, which we will refer to as direction decoupling, is to estimate fluxes across interfaces in a regular array of cells by using a one-dimensional flux expression based on the component of flow velocity normal to the interface between cells. This means that fluxes cannot be exchanged between diagonally adjacent cells since they share no cell interface, even if the local flow conditions dictate that the fluxes should flow diagonally. The direction decoupling imposed by the numerical method requires that the fluxes reach a diagonally adjacent cell in two time-steps.

To evaluate the effects of this direction decoupling, we examine two numerical methods which differ only in that one uses direction decoupling while the other does not. We examine a generalized form of Pullin's equilibrium flux method (EFM) [D.I. Pullin, Direct simulation methods for compressible ideal gas flow, J. Comput. Phys. 34 (1980) 231–244] which we have called the true direction equilibrium flux method (TDEFM). The TDEFM fluxes, derived from kinetic theory, flow not only between cells sharing an interface, but ultimately to any cell in the grid. TDEFM is used here to simulate a blast wave and an imploding flow problem on a structured rectangular mesh and is compared with results from direction decoupled EFM. Since both EFM and TDEFM are identical in the low CFL number limit, differences between the results demonstrate the detrimental effect of direction decoupling. Differences resulting from direction decoupling are also shown in the simulation of hypersonic flow over a rectangular body. The computational cost of allowing the EFM fluxes to flow in the correct directions on the grid is minimal.

PACS: 31.15.Qg; 34.10.+x; 47.10.A−; 47.11.−j; 47.11.Mn; 47.45.Ab; 47.45.−n

Keywords: Computational fluid dynamics; CFD; Kinetic theory of gases; DSMC; Direct simulation

* Corresponding author. Tel.: +886 7 557 1351.
E-mail address: Archembaud@hotmail.com (M.R. Smith).

0021-9991/$ - see front matter
doi:10.1016/j.jcp.2007.12.015

1. Introduction

Bird's Direct Simulation Monte Carlo (DSMC) method [5] simulates a rarefied flow by following the motion and collisions of a large number of simulator particles as they move through the flow. DSMC in the high collision rate limit has been used as an Euler solver [1,6–8] and as the 'continuum' part of a hybrid DSMC/continuum solver. DSMC is generally more robust than a conventional Euler solver but suffers from statistical scatter which requires large amounts of CPU power to reduce to acceptable limits. One reason for DSMC's stability is that the fluxes of mass, momentum and energy are carried by particles which move in the physically correct directions; in any time step fluxes may flow from any cell to any other cell in the computational domain.

In continuum solvers the fluxes are typically 'direction decoupled'; one dimensional flux calculations are performed in the direction normal to the interface between two cells, and the fluxes are only exchanged with cells that share an interface. For example, on a 2D structured grid the fluxes flow in two coordinate directions and never flow in one time step between cells which are diagonally contiguous (share a vertex in common) but do not have a common interface. Cook [9] shows that when the cell structure is not well aligned with the physical structures in the flow, direction decoupled methods may produce non-physical results such as negative temperatures or densities where strong shocks occur or interact. These solvers may also produce asymmetrical results where symmetrical results are theoretically required.

This phenomenon can be demonstrated through the solutions of radially imploding or exploding flows on rectangular meshes. Fig. 1 shows the computational domain and the initial condition in which there is a low pressure cylindrical region surrounded by a high pressure region with a sharp discontinuity between the two. A cylindrically symmetric shock wave will propagate toward the center, causing an increase in temperature and density as the shock travels inwards. The figure also shows density contours found using three existing direction decoupled methods. It can be seen that the direction decoupled methods give asymmetrical results.

Pullin [1] proposed the equilibrium flux method (EFM) in which the fluxes carried by particles having velocities conforming to the local Maxwell–Boltzmann distribution were calculated analytically for the limit of an infinite number of particles. EFM eliminates the statistical scatter associated with the effectively equivalent particle flux methods. When EFM was used in 2D and 3D flows [10–13] the conventional direction decoupling approach described above was used. A 1D solution using EFM to calculate fluxes between cells is presented in Fig. 2. Viscous effects are ignored, although the numerical viscosity inherent to EFM is present. Fig. 2 also shows the radially symmetric density contours as constructed from the 1D solution corresponding to the conditions and elapsed time used in the direction decoupled results shown in Fig. 1.

Since the EFM fluxes are just the amounts of mass, momentum and energy transported by molecules in free-molecular flight there is no need, other than for simplicity, to use direction decoupling when EFM is applied in two or three dimensions. The true direction equilibrium flux method [3,4] represent the analytical expressions for the fluxes carried by molecules originating in a rectangular cell with velocities selected from the Maxwell–Boltzmann distribution and moved in free-flight in a specified time of flight to any rectangular region. One-dimensional TDEFM fluxes are equivalent to EFM fluxes when the CFL number approaches zero. In this limit, the only difference between TDEFM and EFM exists in higher dimensions when EFM is direction decoupled while TDEFM is not. The TDEFM flux expressions are the analytical equivalent to Macrossan et al.'s particle flux method (PFM) [15] applied to rectangular cells.

Here we compare TDEFM results to those obtained from direction decoupled EFM for a 2D implosion problem and a 2D blast wave problem. These differences are then further demonstrated in the simulation of hypersonic flow over a rectangular body. The aim of the paper is to examine the effects of direction coupling alone, thus both methods are restricted to first order accuracy in space and time, using identical grids with identical time steps. Since both solvers share the same underlying principles and differ only in the direction decoupling aspect, results show the detrimental effects due to direction decoupling.

2. Derivation of TDEFM flux expressions

Below are the expressions for the mass, momentum and energy carried by molecules in free-molecular flight for time Δt, starting from a rectangular region (in 2D) to any other rectangular region. All forces acting on

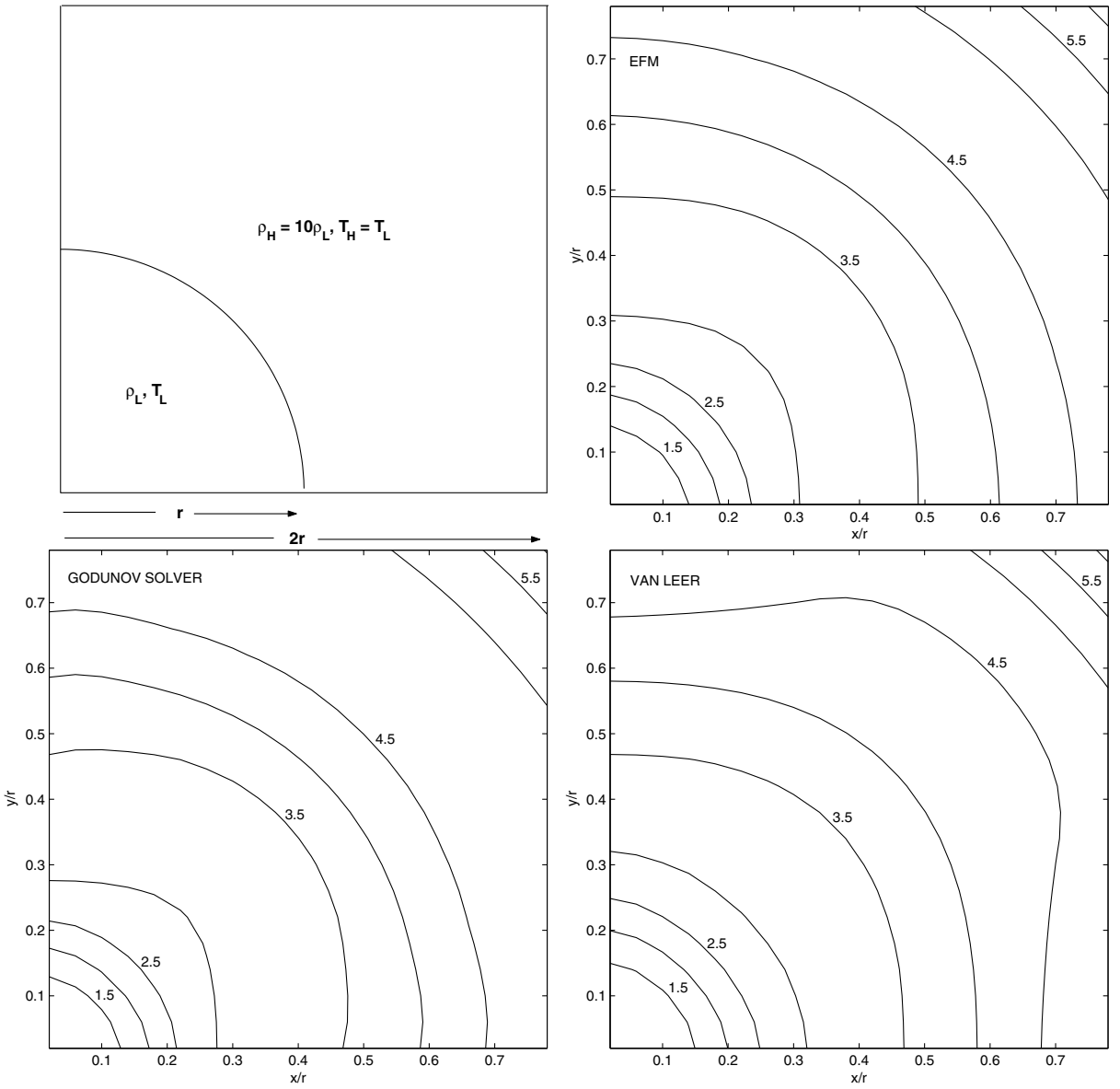

Fig. 1. Direction decoupled 2D solutions to the implosion problem using a 50×50 mesh shown in Fig. 2: (top left) initial condition; (top right) EFM; (lower left) Godunov method [2]; (lower right) Van Leer [14]. Contours are of density (ρ/ρ_L) with contours every 0.5. Flow is shown at $t\sqrt{RT_L}/r = 0.098$ after 100 time steps. Initial conditions are $\gamma = 9/7, T_H/T_L = 1.0, \rho_H/\rho_L = 10$. Computational domain lies in the square region $0 < x/r < 2$.

particles are assumed to be zero, *i.e.* no particle interactions occur while particles are moving. Uniform conditions are assumed within the cell from which the molecules originate (*i.e.* there are no gradients of density, mean velocity or temperature within the cell) and all the molecules within the cell have velocities conforming to the same Maxwell–Boltzmann distribution:

$$g(v_j) = \frac{1}{\sqrt{2\pi}s} \exp\left(\frac{-(v_j - m_j)^2}{2s^2}\right), \tag{1}$$

where $s = (RT)^{0.5}, m_j$ is the bulk velocity and v_j the velocity in the direction j. Referring to Fig. 3, the probability of a particle from location x falling in the region between x_l and x_r in the time Δt is

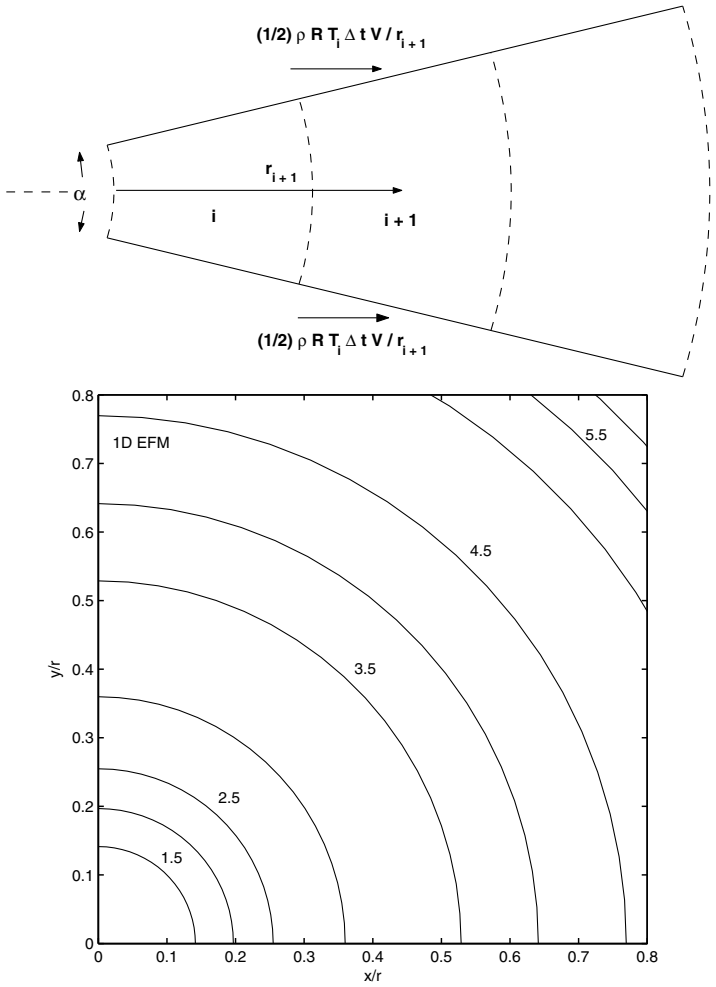

Fig. 2. (Left) Finite volume representation for a 1D simulation showing momentum correction. (Right) Reconstructed 2D solution to the implosion problem using 1D-EFM. Flow is shown at $t\sqrt{RT_L}/r = 0.098$ after 100 time steps. Initial conditions are $\gamma = 9/7$, $T_H/T_L = 1.0, \rho_H/\rho_L = 10$. Computational domain lies in the square region $0 < x/r < 2$.

$$P_m = \int_{\frac{x_l - x}{\Delta t}}^{\frac{x_r - x}{\Delta t}} \frac{1}{\sqrt{2\pi}s} \exp\left(\frac{-(v-m)^2}{2s^2}\right) \mathrm{d}v_x = \frac{1}{2}\left[\mathrm{erf}\left(\frac{m\Delta t + x - x_l}{\sqrt{2}s\Delta t}\right) - \mathrm{erf}\left(\frac{m\Delta t + x - x_r}{\sqrt{2}s\Delta t}\right)\right].$$

The 'mean' probability P_m over the region between x_L and x_R is

$$\begin{aligned} f_M &= \frac{1}{(x_R - x_L)} \int_{x_L}^{x_R} P_m \,\mathrm{d}x = \mathbf{f}_M(m, s, \Delta t, x_R, x_L, x_l, x_r) \\ &= M_c \exp\left(\frac{-(m\Delta t + x_R - x_l)^2}{2s^2\Delta t^2}\right) + M_1 \mathrm{erf}\left(\frac{m\Delta t + x_R - x_l}{\sqrt{2}s\Delta t}\right) - M_c \exp\left(\frac{-(m\Delta t + x_R - x_r)^2}{2s^2\Delta t^2}\right) \\ &\quad - M_2 \mathrm{erf}\left(\frac{m\Delta t + x_R - x_r}{\sqrt{2}s\Delta t}\right) - M_c \exp\left(\frac{-(m\Delta t + x_L - x_l)^2}{2s^2\Delta t^2}\right) - M_3 \mathrm{erf}\left(\frac{m\Delta t + x_L - x_l}{\sqrt{2}s\Delta t}\right) + M_c \\ &\quad \times \exp\left(\frac{-(m\Delta t + x_L - x_r)^2}{2s^2\Delta t^2}\right) + M_4 \mathrm{erf}\left(\frac{m\Delta t + x_L - x_r}{\sqrt{2}s\Delta t}\right), \end{aligned} \tag{2}$$

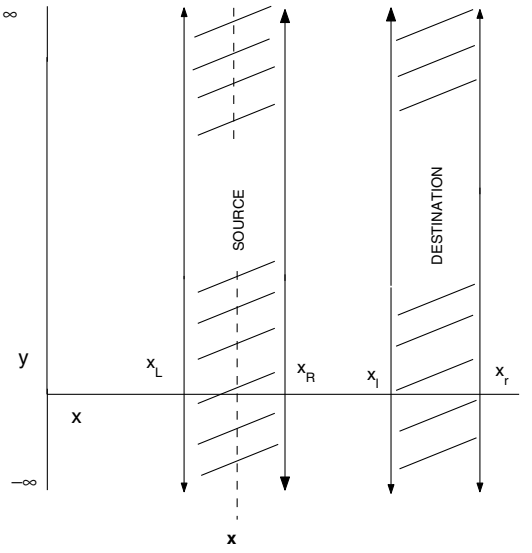

Fig. 3. Particle moving from the source region at x ($x_L \geqslant x \geqslant x_R$) to the destination region between x_l and x_r.

where the values of $M_c, M_1 - M_5$ are located in the Appendix. It is clear that f_M represents the total fraction of mass between the region between x_L and x_R to move into the region between x_l and x_r, and is therefore the mass flux per unit mass from the source region.

The mean velocity of particles from location x to land in the region between x_l and x_r, found by taking the moment of the velocity distribution function, is

$$\begin{aligned} P_p &= \int_{\frac{x_l-x}{\Delta t}}^{\frac{x_r-x}{\Delta t}} \frac{v_x}{\sqrt{2\pi}s} \exp\left(\frac{-(v_x-m)^2}{2s^2}\right) \mathrm{d}v_x = \left[-\frac{s}{\sqrt{2\pi}} \exp\left(\frac{-(m-v_x)^2}{2s^2}\right) - \frac{m}{2}\mathrm{erf}\left(\frac{m-v_x}{\sqrt{2}s}\right)\right]_{\frac{x_l-x}{\Delta t}}^{\frac{x_r-x}{\Delta t}} \\ &= \frac{s}{\sqrt{2\pi}}\left[\exp\left(\frac{-(m\Delta t+x-x_l)^2}{2s^2\Delta t^2}\right) - \exp\left(\frac{-(m\Delta t+x-x_r)^2}{2s^2\Delta t^2}\right)\right] \\ &\quad + \frac{m}{2}\left[\mathrm{erf}\left(\frac{m\Delta t+x-x_l}{\sqrt{2}s\Delta t}\right) - \mathrm{erf}\left(\frac{m\Delta t+x-x_r}{\sqrt{2}s\Delta t}\right)\right]. \end{aligned}$$

The mean average velocity of particles (or the average momentum per unit source mass) moving into region $x_l \leftrightarrow x_r$ from region $x_L \leftrightarrow x_R$ is

$$\begin{aligned} f_P &= \frac{1}{(x_R-x_L)}\int_{x_L}^{x_R} P_p \,\mathrm{d}x = \mathbf{f}_P(m,s,\Delta t,x_R,x_L,x_l,x_r) \\ &= P_c \exp\left(\frac{-(m\Delta t+x_R-x_l)^2}{2s^2\Delta t^2}\right) + P_1\mathrm{erf}\left(\frac{m\Delta t+x_R-x_l}{\sqrt{2}s\Delta t}\right) - P_c \exp\left(\frac{-(m\Delta t+x_R-x_r)^2}{2s^2\Delta t^2}\right) \\ &\quad - P_2\mathrm{erf}\left(\frac{m\Delta t+x_R-x_r}{\sqrt{2}s\Delta t}\right) - P_c \exp\left(\frac{-(m\Delta t+x_L-x_l)^2}{2s^2\Delta t^2}\right) - P_3\mathrm{erf}\left(\frac{m\Delta t+x_L-x_l}{\sqrt{2}s\Delta t}\right) \\ &\quad + P_c \exp\left(\frac{-(m\Delta t+x_L-x_r)^2}{2s^2\Delta t^2}\right) + P_4\mathrm{erf}\left(\frac{m\Delta t+x_L-x_r}{\sqrt{2}s\Delta t}\right), \end{aligned} \tag{3}$$

where the values of $P_c, P_1 - P_5$ are located in the Appendix. The energy carried by a particle, in any single simulated direction, can be divided into a kinetic energy and internal energy:

$$E_p = \frac{1}{2}v^2 + C,$$
$$C \equiv \frac{1}{2\zeta}\left(\frac{2}{\gamma - 1} - \zeta\right)s^2, \tag{4}$$

where C is the internal energy per simulated degrees of freedom ζ, thus $\zeta = 2$ in a 2D simulation. This 'internal energy' includes contributions from rotation and vibration, as well as contributions from unused translational degrees of freedom as proposed by Pullin [1]. Therefore, there is no limit upon which value of γ can be used. Therefore, the mean energy of particles (per unit mass) moving from x into the region between x_l and x_r, P_e, is defined as

$$\begin{aligned}
P_e &= \int_{\frac{x_l - x}{\Delta t}}^{\frac{x_r - x}{\Delta t}} \frac{(0.5v_x^2 + C)}{\sqrt{2\pi}s} \exp\left(\frac{-(v_x - m)^2}{2s^2}\right) \mathrm{d}v_x \\
&= \left[\frac{(m^2 + s^2 + 2C)}{4}\mathrm{erf}\left(\frac{v_x - m}{\sqrt{2}s}\right) - \frac{s(m + v_x)}{2\sqrt{2\pi}} \exp\left(\frac{-(m - v_x)^2}{2s^2}\right)\right]_{\frac{x_l - x}{\Delta t}}^{\frac{x_r - x}{\Delta t}} \\
&= \frac{(2C + m^2 + s^2)}{4}\left[\mathrm{erf}\left(\frac{m\Delta t + x - x_l}{\sqrt{2}s\Delta t}\right) - \mathrm{erf}\left(\frac{m\Delta t + x - x_r}{\sqrt{2}s\Delta t}\right)\right] \\
&\quad + \frac{s(m\Delta t - x + x_l)}{2\sqrt{2\pi}\Delta t} \exp\left(\frac{-(m\Delta t + x - x_l)^2}{2s^2\Delta t^2}\right) - \frac{s(m\Delta t - x + x_r)}{2\sqrt{2\pi}\Delta t} \exp\left(\frac{-(m\Delta t + x - x_r)^2}{2s^2\Delta t^2}\right).
\end{aligned}$$

The mean energy over the range x_L to x_R to flow into the region between x_l and x_r is

$$\begin{aligned}
f_E &= \frac{1}{(x_R - x_L)} \int_{x_L}^{x_R} P_e \,\mathrm{d}x = \mathbf{f}_E(m, s, \Delta t, x_R, x_L, x_l, x_r \\
&= E_c \exp\left(\frac{-(m\Delta t + x_R - x_l)^2}{2s^2\Delta t^2}\right) + E_1 \mathrm{erf}\left(\frac{m\Delta t + x_R - x_l}{\sqrt{2}s\Delta t}\right) - E_c \exp\left(\frac{-(m\Delta t + x_R - x_r)^2}{2s^2\Delta t^2}\right) \\
&\quad - E_2 \mathrm{erf}\left(\frac{m\Delta t + x_R - x_r}{\sqrt{2}s\Delta t}\right) - E_c \exp\left(\frac{-(m\Delta t + x_L - x_l)^2}{2s^2\Delta t^2}\right) - E_3 \mathrm{erf}\left(\frac{m\Delta t + x_L - x_l}{\sqrt{2}s\Delta t}\right) \\
&\quad + E_c \exp\left(\frac{-(m\Delta t + x_L - x_r)^2}{2s^2\Delta t^2}\right) + E_4 \mathrm{erf}\left(\frac{m\Delta t + x_L - x_r}{\sqrt{2}s\Delta t}\right),
\end{aligned} \tag{5}$$

where the values of $E_c, E_1 - E_5$ are located in the Appendix. These fluxes expressions are first order accurate in time and space – this is done to ensure fair comparison with the EFM fluxes. Higher order implementations of TDEFM may be implemented though:

- The application of a normalised, linearly varying flow properties e.g. $\rho(x)$ ($\rho(x, y)$ in higher dimensions) prior to integration over the source region. This is then integrated over the source volume to determine the fluxes of mass, momentum and energy per unit mass. There are currently analytical expressions available when density and velocity gradients are applied this way [4].
- The application of arbitrarily selected reconstructions of flow properties to provide improved estimates of conditions at the volume boundaries can be used to calculate pseudo-direction coupled fluxes. These conditions are used to calculate one-dimensional fluxes which are then transported to all neighbouring cells, including those diagonally adjacent.

Other flow properties can be applied to the flux calculation procedure in the same way. Careful selection of the function $\rho(x, y)$ allows mathematical splitting of the expressions [4]. While this is not difficult to achieve, it is beyond the scope of investigating the effects of direction decoupling and will not be investigated here.

3. TDEFM fluxes in the low CFL number limit

Instead of using a region of finite width into which the fluxes flow (as used in Eqs. (2)–(4)), we can use a right-hand bound infinitely far away from the source region and take the limit $\Delta t \to 0$.

Using Eq. (2), with the right-hand side of the destination region x_r set to ∞, now becomes

$$f_M = \frac{Z}{2\sqrt{\pi}}\left[\exp(-S^2) - \exp\left(-\left(S-\frac{1}{Z}\right)^2\right)\right] + \frac{1}{2}SZ\left[\operatorname{erf}(S) - \operatorname{erf}\left(S-\frac{1}{Z}\right)\right] + \frac{1}{2}\left[\operatorname{erf}\left(S-\frac{1}{Z}\right)+1\right] \quad (6)$$

where the speed ratio $S = \frac{m}{c_{mp}}$, $c_{mp} \equiv \sqrt{2RT}$ is the most probable speed, and $Z \equiv \frac{\Delta t\sqrt{2RT}}{\Delta x} = \frac{\Delta t c_{mp}}{\Delta x}$. This equation represents the reduced TDEFM mass flux expression when the destination and source cells are adjacent. Further simplifications are possible in the low CFL limit. Recalling that $\operatorname{erf}(-\infty) = -1$ and $\exp(-\infty) = 0$ the expression becomes

$$f_M = \frac{\Delta t}{\Delta x}\left[\frac{c_{mp}}{2\sqrt{\pi}}\exp(-S^2) + m\left[\frac{1}{2}\operatorname{erf}(S) + \frac{1}{2}\right]\right]. \quad (7)$$

The actual mass to move from the source region to the destination region per unit time per unit area is

$$M = \frac{M_o f_M}{A\Delta t} = \rho\left[\frac{c_{mp}}{2\sqrt{\pi}}\exp(-S^2) + m\left[\frac{1}{2}\operatorname{erf}(S) + \frac{1}{2}\right]\right]. \quad (8)$$

This equation is identical to the EFM mass flux. Likewise treatment of momentum and energy fluxes also provide the EFM fluxes in the small time step limit. The difference between the EFM and TDEFM fluxes only becomes significant when the kinetic CFL number is larger than 1. The kinetic CFL number is defined here as

$$\mathrm{CFL} = \frac{(|m| + \sigma s)\Delta t}{\Delta x}, \quad (9)$$

where σ is a selected number of variances of the equilibrium distribution. At a CFL of 0.1, with $\sigma = 5$, used as an upper limit throughout this paper, the maximum difference between the density profiles found in a simple 1D test (shown in Fig. 4) is 1e−13%. At a kinetic CFL number of 1, this difference increases to 1.5%. We therefore conclude that the use of the simplified of TDEFM in the low CFL number limit is justified.

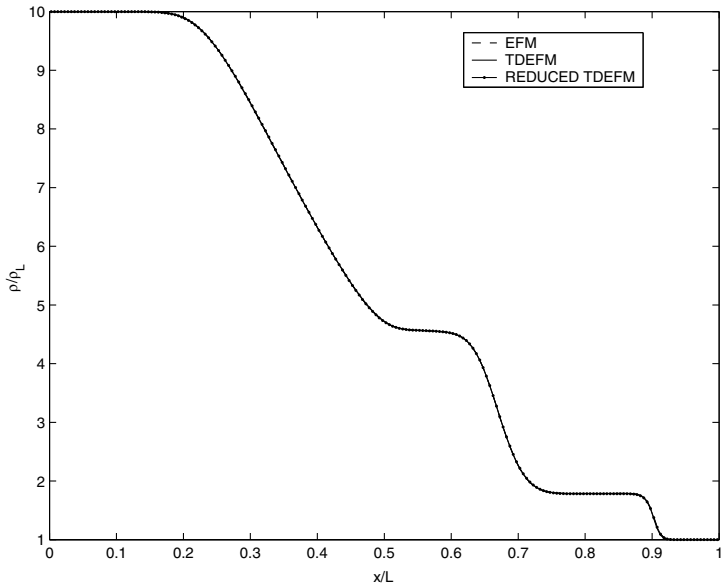

Fig. 4. Density profiles taken from various solvers for the 1D shock tube problem. At time $t = 0$, an imaginary diaphragm separating gases with a density ratio of 10 and a temperature ratio of 1 is removed. The gas is initially at rest, is assumed inviscid and is ideal with $\gamma = 5/3$.

4. Implementation of TDEFM in two and three dimensions

Referring to Fig. 5, the net flux of mass, momentum and energy to move from the source region to the destination region is

$$
\begin{aligned}
M &= M_0 \mathbf{f}_M\left(U, \sqrt{RT}, \Delta t, x_R, x_L, x_l, x_r\right) \times \mathbf{f}_M\left(V, \sqrt{RT}, \Delta t, y_R, y_L, y_l, y_r\right),\\
P_x &= M_0 \mathbf{f}_P\left(U, \sqrt{RT}, \Delta t, x_R, x_L, x_l, x_r\right) \times \mathbf{f}_M\left(V, \sqrt{RT}, \Delta t, y_R, y_L, y_l, y_r\right),\\
P_y &= M_0 \mathbf{f}_M\left(U, \sqrt{RT}, \Delta t, x_R, x_L, x_l, x_r\right) \times \mathbf{f}_P\left(V, \sqrt{RT}, \Delta t, y_R, y_L, y_l, y_r\right),\\
E_x &= M_0 \mathbf{f}_E\left(U, \sqrt{RT}, \Delta t, x_R, x_L, x_l, x_r\right) \times \mathbf{f}_M\left(V, \sqrt{RT}, \Delta t, y_R, y_L, y_l, y_r\right),\\
E_y &= M_0 \mathbf{f}_M\left(U, \sqrt{RT}, \Delta t, x_R, x_L, x_l, x_r\right) \times \mathbf{f}_E\left(V, \sqrt{RT}, \Delta t, y_R, y_L, y_l, y_r\right),\\
E &= E_x + E_y,
\end{aligned}
$$

where M, P and E are the net mass, momentum and energy fluxes respectively, M_0 is the initial mass in the source region, and $([x_L, y_L], [x_R, y_R])$ give the size and location of the rectangular source region, $([x_l, y_l], [x_r, y_r])$ describe the size and location of the destination region, U is the X velocity, V is the Y velocity, M is the net mass flux, P_x and P_y are the X and Y momentum fluxes and E is the energy flux. For the extension to 3D, the process is very simple. The fluxes of mass, momentum and energy from the source cell to the destination cell, shown in Fig. 6, is

$$
\begin{aligned}
M &= M_0 \mathbf{f}_M\left(U, \sqrt{RT}, \Delta t, x_R, x_L, x_l, x_r\right) \times \mathbf{f}_M\left(V, \sqrt{RT}, \Delta t, y_R, y_L, y_l, y_r\right), \times \mathbf{f}_M\left(Z, \sqrt{RT}, \Delta t, z_R, z_L, z_l, z_r\right),\\
P_x &= M_0 \mathbf{f}_P\left(U, \sqrt{RT}, \Delta t, x_R, x_L, x_l, x_r\right) \times \mathbf{f}_M\left(V, \sqrt{RT}, \Delta t, y_R, y_L, y_l, y_r\right), \times \mathbf{f}_M\left(Z, \sqrt{RT}, \Delta t, z_R, z_L, z_l, z_r\right),\\
P_y &= M_0 \mathbf{f}_M\left(U, \sqrt{RT}, \Delta t, x_R, x_L, x_l, x_r\right) \times \mathbf{f}_P\left(V, \sqrt{RT}, \Delta t, y_R, y_L, y_l, y_r\right), \times \mathbf{f}_M\left(Z, \sqrt{RT}, \Delta t, z_R, z_L, z_l, z_r\right),
\end{aligned}
$$

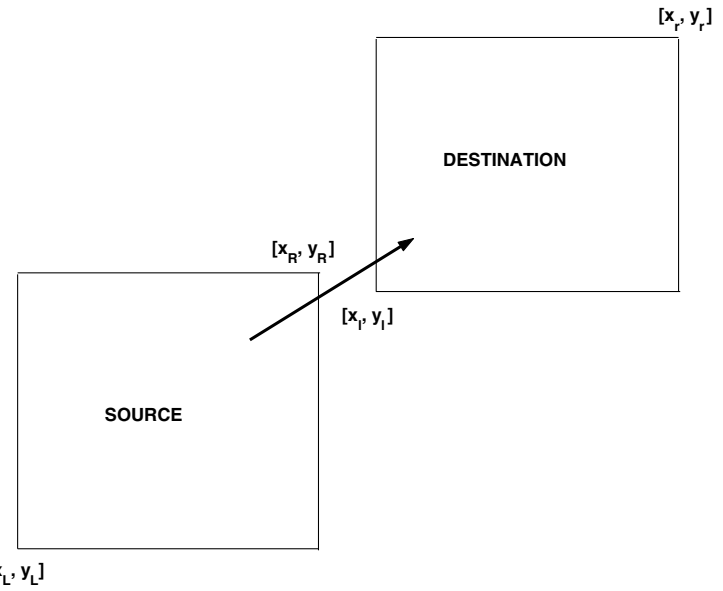

Fig. 5. Sample source and destination cell geometry in 2D. The source cell is bounded by the coordinates $(x_L, y_L) - (x_R, y_R)$. The destination cell is bounded by the coordinates $(x_l, y_l) - (x_r, y_r)$.

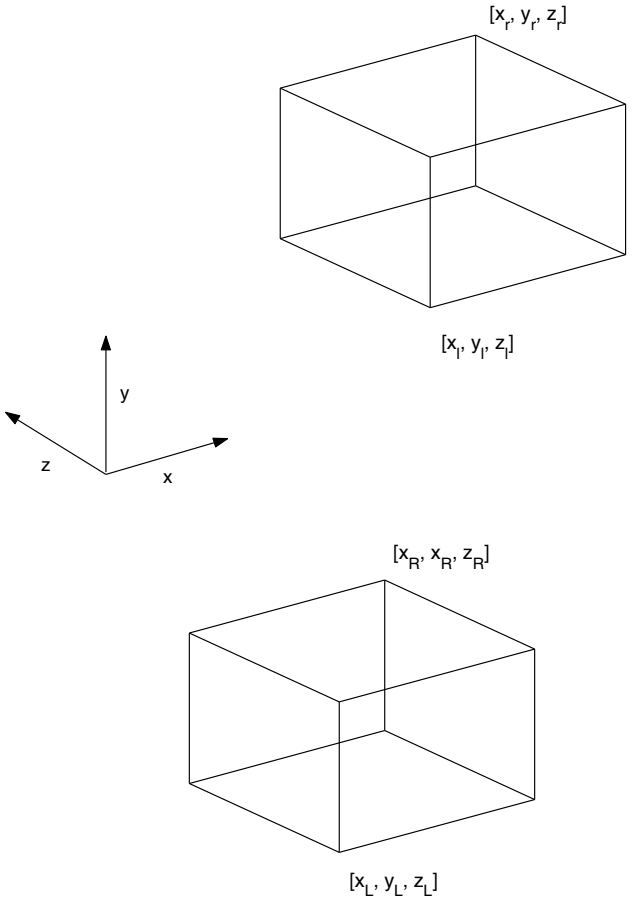

Fig. 6. Sample source and destination cell geometry in 3D. The source cell is bounded by the coordinates $(x_L, y_L, z_L) - (x_R, y_R, z_R)$. The destination cell is bounded by the coordinates $(x_l, y_l, z_l) - (x_r, y_r, z_r)$.

$$
\begin{aligned}
P_z &= M_0 \mathbf{f}_M\left(U, \sqrt{RT}, \Delta t, x_R, x_L, x_l, x_r\right) \times \mathbf{f}_M\left(V, \sqrt{RT}, \Delta t, y_R, y_L, y_l, y_r\right), \times \mathbf{f}_P\left(Z, \sqrt{RT}, \Delta t, z_R, z_L, z_l, z_r\right), \\
E_x &= M_0 \mathbf{f}_E\left(U, \sqrt{RT}, \Delta t, x_R, x_L, x_l, x_r\right) \times \mathbf{f}_M\left(V, \sqrt{RT}, \Delta t, y_R, y_L, y_l, y_r\right), \times \mathbf{f}_M\left(Z, \sqrt{RT}, \Delta t, z_R, z_L, z_l, z_r\right), \\
E_y &= M_0 \mathbf{f}_M\left(U, \sqrt{RT}, \Delta t, x_R, x_L, x_l, x_r\right) \times \mathbf{f}_E\left(V, \sqrt{RT}, \Delta t, y_R, y_L, y_l, y_r\right), \times \mathbf{f}_M\left(Z, \sqrt{RT}, \Delta t, z_R, z_L, z_l, z_r\right), \\
E_z &= M_0 \mathbf{f}_M\left(U, \sqrt{RT}, \Delta t, x_R, x_L, x_l, x_r\right) \times \mathbf{f}_M\left(V, \sqrt{RT}, \Delta t, y_R, y_L, y_l, y_r\right), \times \mathbf{f}_E(Z, \sqrt{RT}, \Delta t, z_R, z_L, z_l, z_r), \\
E &= E_x + E_y + E_z.
\end{aligned}
$$

Significant simplifications of these flux expressions can be performed when the computational domain is a simple cartesian mesh, as displayed in Fig. 7. To calculate the mass fluxes from the source cell (in the region $x_L \geqslant x \geqslant x_R, y_L \geqslant y \geqslant y_R$) to all surrounding cells, only four total evaluations of f_M are required. The flux calculation procedure for the mass fluxes is

(1) Calculate values of f_N, f_S, f_E and f_W. In this instance, these values are

$$f_N = \mathbf{f}_M\left(V, \sqrt{RT}, \Delta t, y_R, y_L, y_R, y_r\right),$$

$$f_S = \mathbf{f}_M\left(V, \sqrt{RT}, \Delta t, y_R, y_L, y_l, y_L\right),$$

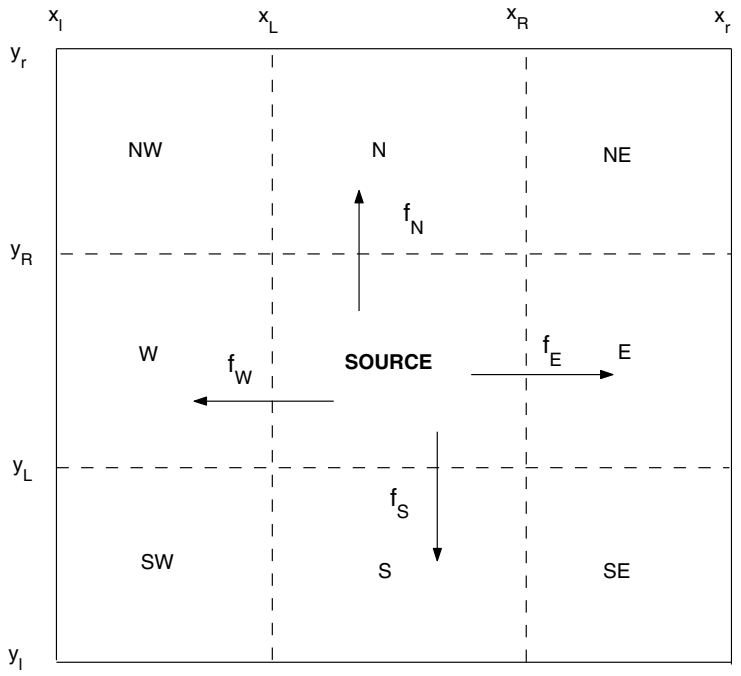

Fig. 7. Diagram showing source cell (in center) surrounded by destination cells.

$$f_E = \mathbf{f}_M\left(U, \sqrt{RT}, \Delta t, x_R, x_L, x_R, x_r\right),$$
$$f_W = \mathbf{f}_M\left(U, \sqrt{RT}, \Delta t, x_R, x_L, x_l, x_L\right).$$

If we assume that (i) the local CFL is small, and (ii) that all of the mass is captured in the surrounding cells, the expressions for these fluxes simplify to Pullin's EFM fluxes, requiring only a single erf( ) and exp( ) function evaluation each.

(2) Making use of the above assumptions, the fluxes of mass to the surrounding neighbours are

$$M_{NW} = M_0 \times f_N \times f_W,$$
$$M_N = M_0 \times f_N \times (1 - f_W - f_E),$$
$$M_{NE} = M_0 \times f_N \times f_E,$$
$$M_W = M_0 \times (1 - f_N - f_S) \times f_W,$$
$$M_E = M_0 \times (1 - f_N - f_S) \times f_E,$$
$$M_{SW} = M_0 \times f_S \times f_W,$$
$$M_S = M_0 \times f_S \times (1 - f_W - f_E),$$
$$M_{SE} = M_0 \times f_S \times f_E.$$

This procedure can be repeated for the momentum and energy fluxes. This procedure reduces the computational expense significantly, with this form of TDEFM requiring 10% more computational time that ordinary EFM. If required, the "cell catchment" region could be increased to include more distant cells; however this would mean that the flow might posses an artificially large mean free path. In hypersonic flow, if the bulk velocity in a cell is larger than $3\sqrt{RT}$, the contribution from cells downstream would be negligible and can be disregarded. In the results presented here, the time step is limited to ensure that all of the mass is captured in the surrounding 8 cells and the reduced form of the TDEFM flux expressions are used. To demonstrate the effect of direction decoupling, a strictly uniform cartesian grid is used. The implementation of TDEFM on non-rectangular grids is beyond the scope of this investigation.

5. Blast wave problem

The flow field contains a two-dimensional 'blast wave' caused by an initial small region with a temperature higher than the surrounding gas. One quarter of a square plane of unit width with symmetry condition applied on all four walls is used. The length of computational domain is $50r$ in each direction, where r is the radius of the high temperature region. The initial conditions are

$$\begin{aligned} &\rho_H/\rho_L = 1, \\ &T = \chi T_H, \\ &\chi = f + (1-f)\frac{T_L}{T_H}, \\ &U = V = 0, \\ &\gamma = \frac{5}{3}, \end{aligned} \tag{10}$$

where ρ_0 is the density, T_H is the temperature inside the ideal circular initial condition, T_L is the temperature outside. The fraction of the area of each cell inside the high temperature region is given by f, and is demonstrated in Fig. 8. The ratio *chi* is used to ensure that, regardless of mesh density, the initial computational do-

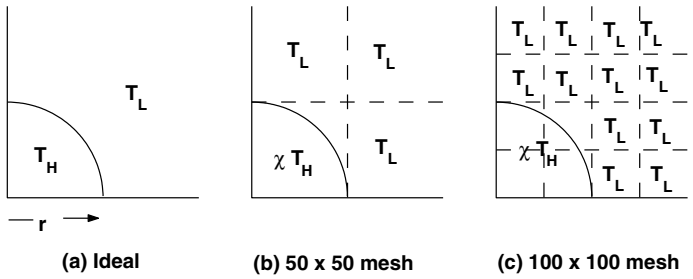

Fig. 8. Blast wave geometry. (a) Ideal initial condition and geometry. (b) Geometry used by the solvers with 50×50 cells. (c) Geometry used by solvers with 100×100 cells. The symmetry boundary condition (specular reflection) was applied at all boundaries. Perfect gas with ratio of specific heats $\gamma = 5/3$. Initial conditions: $T_H/T_L = 1000$, $\rho_H/\rho_L = 1$ (pressure ratio $P_H/P_L = 1000$). Radius of high pressure region is r.

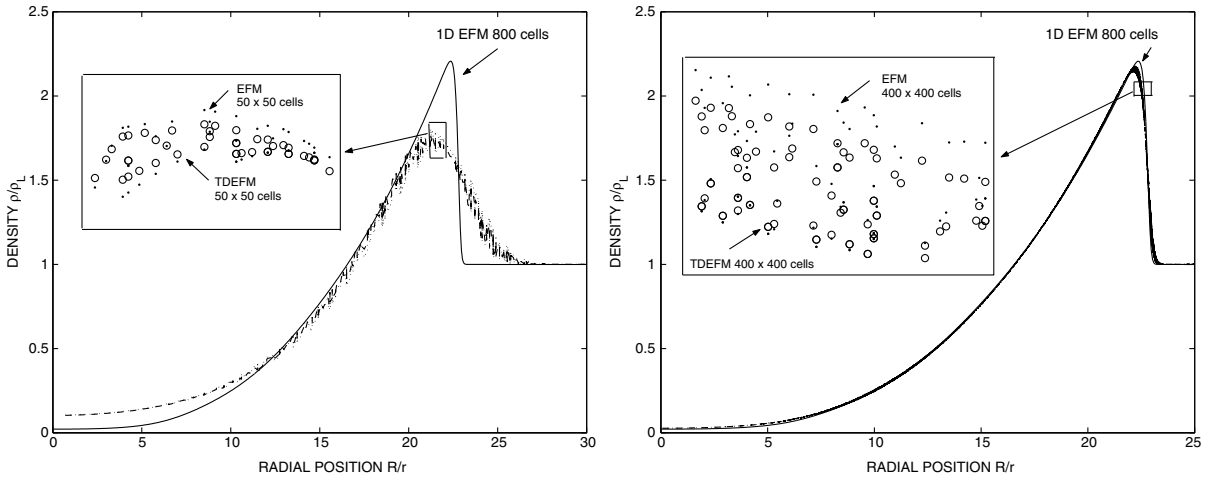

Fig. 9. 2D solutions of the blast wave problem showing normalised density using 2D-TDEFM (○) and 2D-EFM (·) using a 50×50 mesh (left) and a 400×400 mesh (right). The initial conditions as shown in Fig. 8(b). The results from all individual cells are shown and should collapse into a single line. The solid line shows 1D results with 1×800 cells. Simulations are run up to $t\sqrt{RT}/r = 0.00196$. Sections of the results have been enlarged to better demonstrate the scatter present in the results.

main possesses the same total energy. This initial high temperature (and hence pressure) in the one cell simulates a sudden 'explosion' centered on the origin. Ideally, the resulting flow is radially symmetric. The unsteady simulation is run to time $t\sqrt{RT_L}/r = 0.00196$ where the expanding shock wave has traveled to just beyond $22r$. Although the method disregards viscous effects, the same numerical viscosity present in EFM is present in TDEFM.

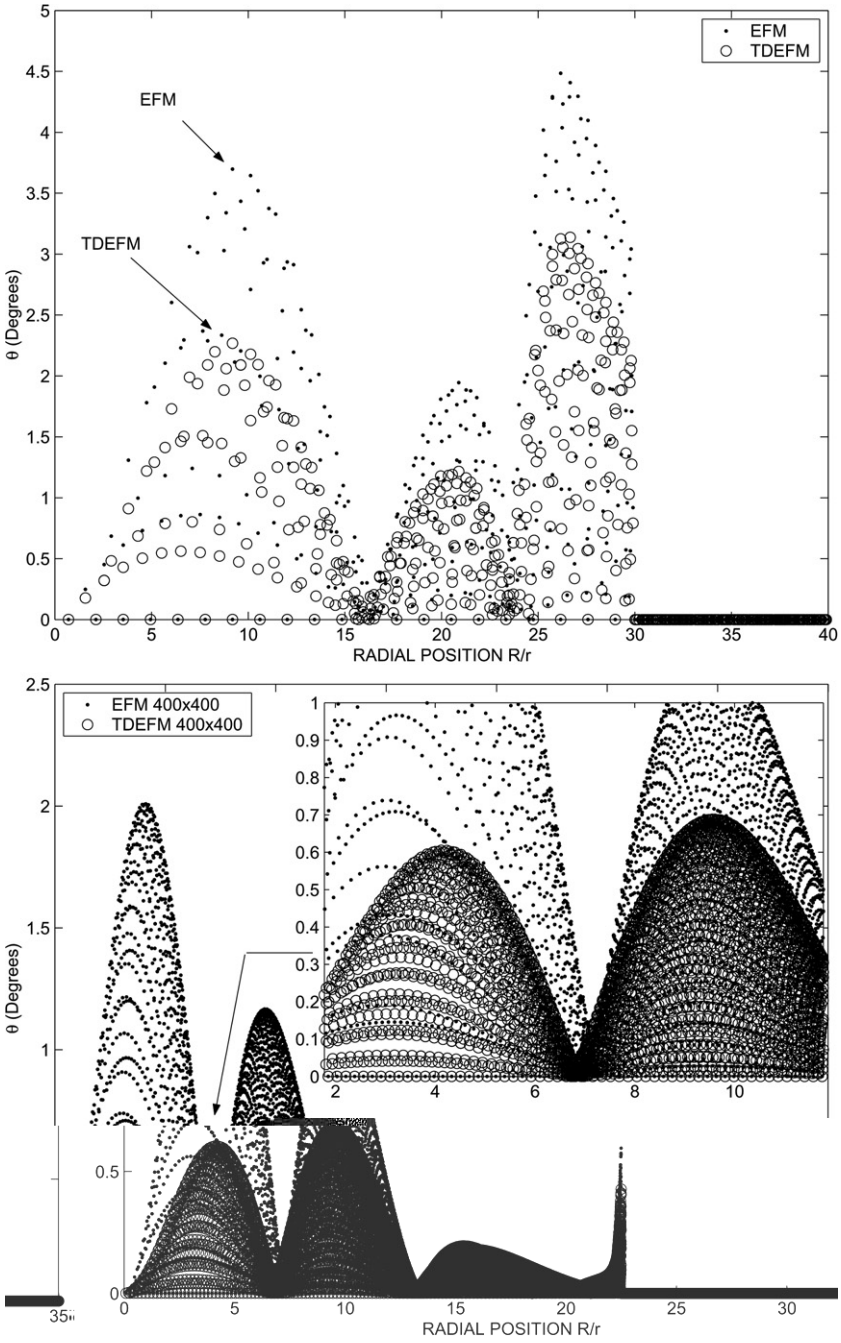

Fig. 10. Angle of deviation for 2D-TDEFM and 2D-EFM for each cell versus radial position in the blast wave problem. (Top) 50×50 cells, (Bottom) 400×400 cells. Simulations are run up to $t\sqrt{RT}/r = 0.00196$. Each point represents the angle of deviation (*i.e.* the angular difference between the radial position vector and the velocity vector) for a given cell.

The benchmark result is obtained from a 1D-EFM solution using the initial condition described in Fig. 8(a). The length of the circular region was divided radially into 800 cells and the simulation run up to $t\sqrt{RT_o}/r = 0.00196$ using 1000 time steps. The benchmark results are represented as solid lines in Fig. 9. Representations of the initial circular starting condition are shown in Fig. 8(a). Fig. 9 shows the normalised density for the 2D-TDEFM and 2D-EFM results for a mesh using 50×50 cells and 400×400 cells. The expected features of this flow are present in both results – an increase in Mach number, density and temperature occur through the radially expanding shock. The flow is smeared due to the inability of the solvers to accurately capture the flow on a coarse mesh, though this smearing diminishes as the mesh density increases. Since the flow is expected to display radial symmetry there is a single correct value for temperature, density and Mach number at any given radius. It can be seen that this is not true for the numerical solution – indeed, the degree of scatter in these profiles is an indication of the error of the solution and has been used as such previously [3].

In order to quantify the effect of direction decoupling, we use an "angle of deviation", designated as θ, to measure the radial symmetry present in the solution. The angle of deviation is defined as the angle between the radial position vector $\vec{r} = (x\boldsymbol{i} + y\boldsymbol{j})$ and the velocity vector $\vec{v} = (V_x\boldsymbol{i} + V_y\boldsymbol{j})$, and is given by

$$\theta = \cos^{-1}\left(\frac{\vec{v}\cdot\vec{r}}{|\vec{r}||\vec{v}|}\right). \tag{11}$$

This angle should be zero because of the radially symmetric nature of the flow. The magnitude of θ at any position is a measure of radial asymmetry in the flow and therefore a measure of error. Fig. 10 shows that deviation angle θ taken from the 2D-EFM and 2D-TDEFM results with meshes of 50×50 and 400×400 cells. It is clear that the angle of deviation is consistently less for TDEFM than for EFM, indicating a higher level of fidelity. This fact remains true regardless of mesh density - simulations using much finer meshes ($\gg$2 million cells) have revealed that the magnitude of the angle of deviation is always lower in TDEFM results than in EFM results. Therefore, there is always an effect due to direction coupling, regardless of mesh density, although this effect diminishes as mesh density increases.

6. Implosion problem

TDEFM has been compared to EFM in a 2D implosion problem with the aim of demonstrating the problems associated with direction splitting. The implosion problem is shown in the introduction in Fig. 1. The initial conditions are as follows:

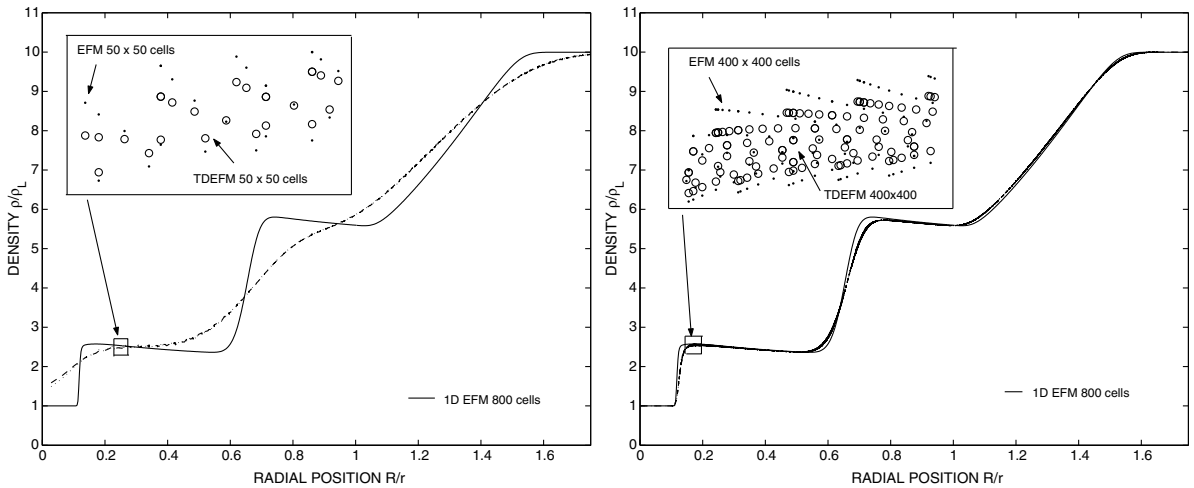

Fig. 11. Two-dimensional solutions to the implosion problem showing normalised density using 2D-TDEFM (○) and 2D-EFM (·) using a 50×50 mesh (left) and a 400×400 mesh (right). The solid line shows 1D results with 1×800 cells. Simulations are run up to $t\sqrt{RT}/r = 0.098$.

$$\rho = \chi \rho_H,$$
$$\chi = f + (1-f)\frac{\rho_L}{\rho_H},$$
$$T_H/T_L = 1,$$

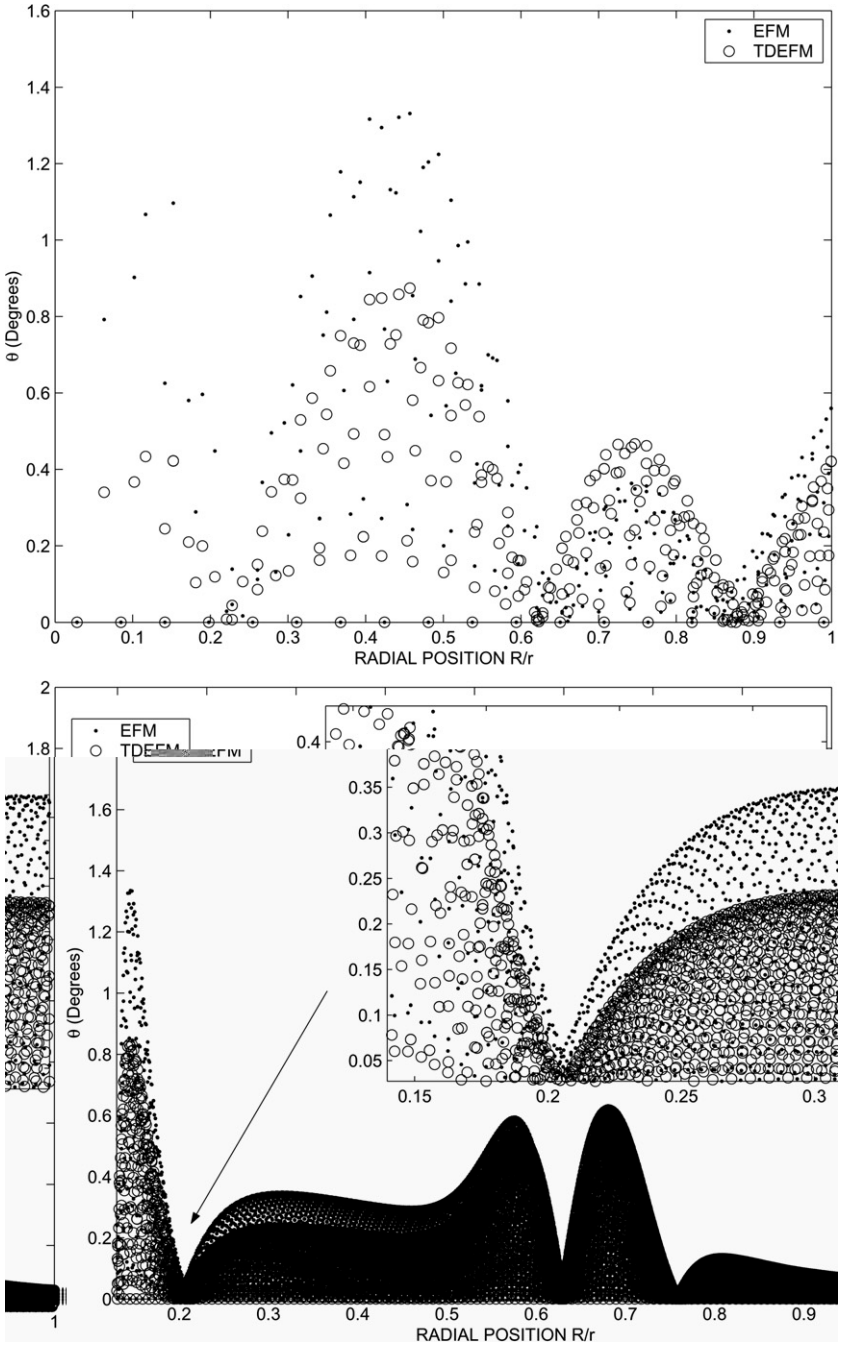

Fig. 12. Angle of deviation for 2D-TDEFM and 2D-EFM in the implosion problem. (top) 50×50 cells, (bottom) 400×400 cells. Simulations are run up to $t\sqrt{RT}/r = 0.098$. Each point represents the angle of deviation (*i.e.* the angular difference between the radial position vector and the velocity vector) for a given cell.

$$U = V = 0,$$
$$\gamma = \frac{5}{3}, \tag{12}$$

where f is the fraction of the cell falling outside radius r. The results from 2D-TDEFM and 2D-EFM using a 50×50 and 400×400 mesh are shown in Fig. 11. As expected, the fine mesh results more closely match the 1D results. The angle of deviation is used again as a measure of radial asymmetry and is shown in

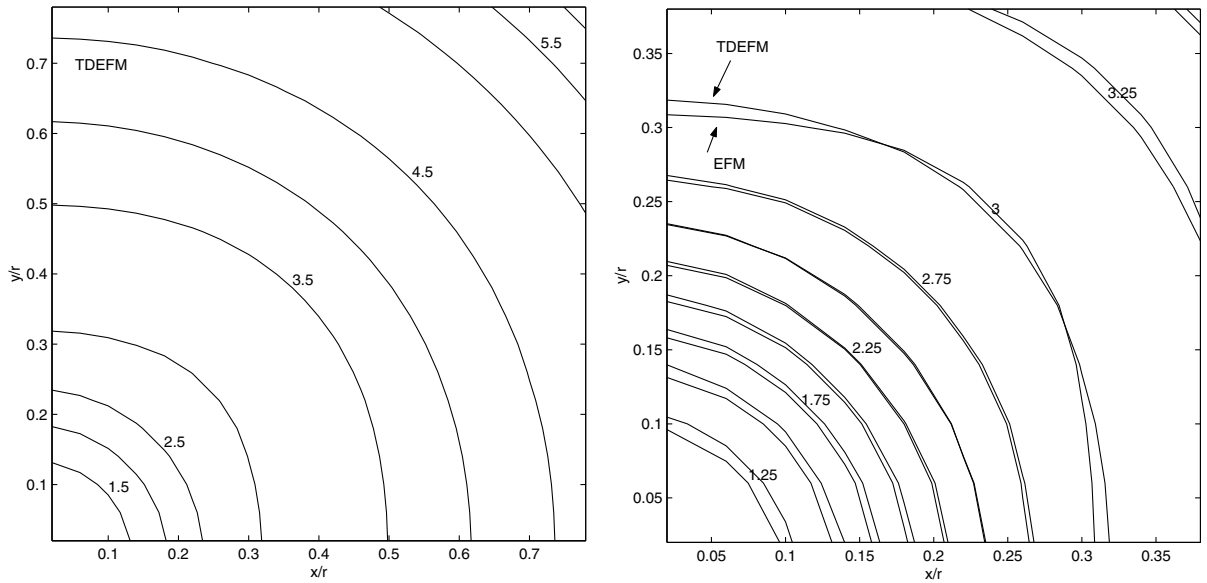

Fig. 13. (Left) Contours of density for the implosion problem shown in Fig. 1 using 2D-TDEFM, (right) enlarged (2×) comparison between contours of density from TDEFM and EFM using the same initial conditions showing the effects of direction decoupling.

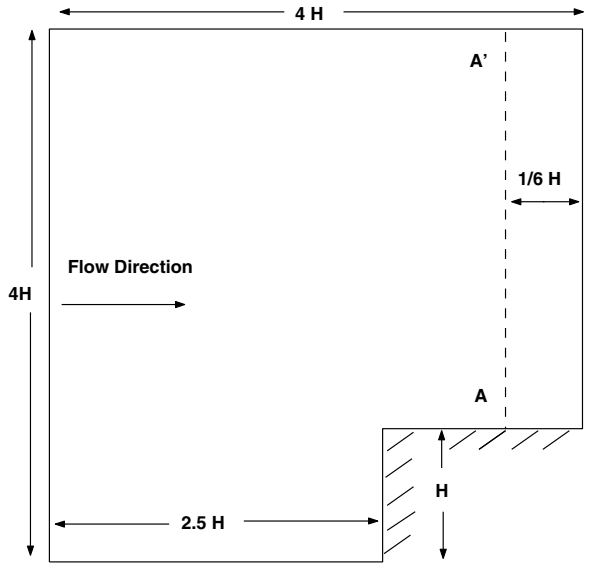

Fig. 14. The computational domain used for the hypersonic flow example over a rectangular body of height H. Flow is at Mach 20 with $\gamma = 1.4$. Initial conditions are $\rho = \rho_\infty, M = M_\infty$ and $T = T_\infty$. The simulations are progressed in time to $t\sqrt{RT_\infty}/H = 3$.

Fig. 12. The angle of deviation is the angular difference between the radial position vector and the velocity vector for any given cells. Fig. 12 shows that 2D-TDEFM gives a more radially symmetric result than 2D-EFM on the same mesh. Shown in Fig. 13 is a comparison of density contours between 2D-EFM and 2D-TDEFM for the same initial conditions used to obtain the results in Fig. 1. The 2D-TDEFM contours are closer to being radially symmetric than the 2D-EFM contours, confirming the result obtained through the analysis of the angle of deviation. The time step used was small enough to justify the simplification of the primary TDEFM flux expressions in Eqs. (2)–(4) to the original EFM expressions. At this time step, the direction coupled EFM provided identical results (differences of less than 1e−13%) to the complete TDEFM expressions while performing the same number of exponential and error function evaluations as direction decoupled EFM.

7. Hypersonic flow over a rectangular body

The previous examples dealt with predominately low speed, unsteady flows in a square region. The results for steady hypersonic flow over the rectangular body shown in Fig. 14 are shown here. The flow conditions are $M_\infty = 20, \rho_\infty = 1$ and $T_\infty = 1$. The flow is progressed until $t\sqrt{RT_\infty}/H = 3$. The gas is ideal with $\gamma = 7/5$. Density contours of the result obtained using TDEFM is shown in Fig. 15. The top and right-hand side boundaries are extrapolated outflow. The lower boundary and the body surfaces are reflective boundaries which are appropriate for this inviscid calculation. As expected, a detached bow shock has formed, with the density increasing through the bow shock and decreasing as the flow expands around the corner of the rectangular body. There are no bumps or other spurious oscillations present in the bow shock.

The temperature and density profiles alone line A–A′ (shown in Fig. 14) are shown in Fig. 16. Here, we can see that even for steady flow problems there is a distinct difference in the solutions. The location at which the detached bow shock crosses the line A–A′ differs for true direction and direction decoupled fluxes. This is true regardless of mesh density. As shown by the density profile in Fig. 16, when the number

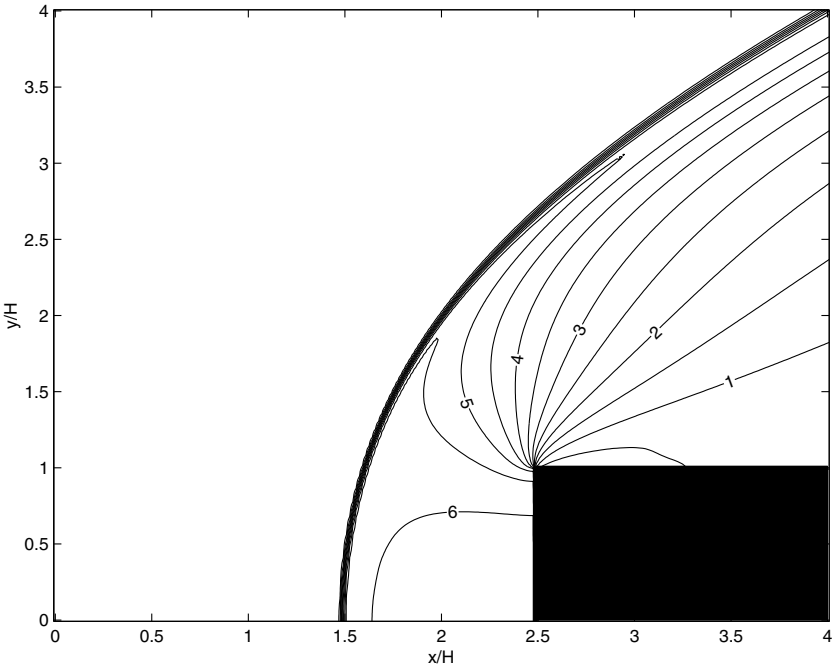

Fig. 15. Colour contours of density for hypersonic flow over a rectangular body of height H using TDEFM. The computational region extends to $4H$, with the front of the body located at $[2.5H, 0]$. Flow is at Mach 20 with $\gamma = 1.4$. Initial conditions are $\rho = \rho_\infty, M = M_\infty$ and $T = T_\infty$. The simulations are progressed in time to $t\sqrt{RT_\infty}/H = 3$.

of cells is increased by more than 400% there is still a noticeable difference in the location of the bow shock. The effect of direction decoupling here is quite severe as the flow is not aligned with the grid. The temperature profile in Fig. 16 extends from $1 \geqslant y/H \geqslant 2.5$ (along the line A–A′ shown in Fig. 14)

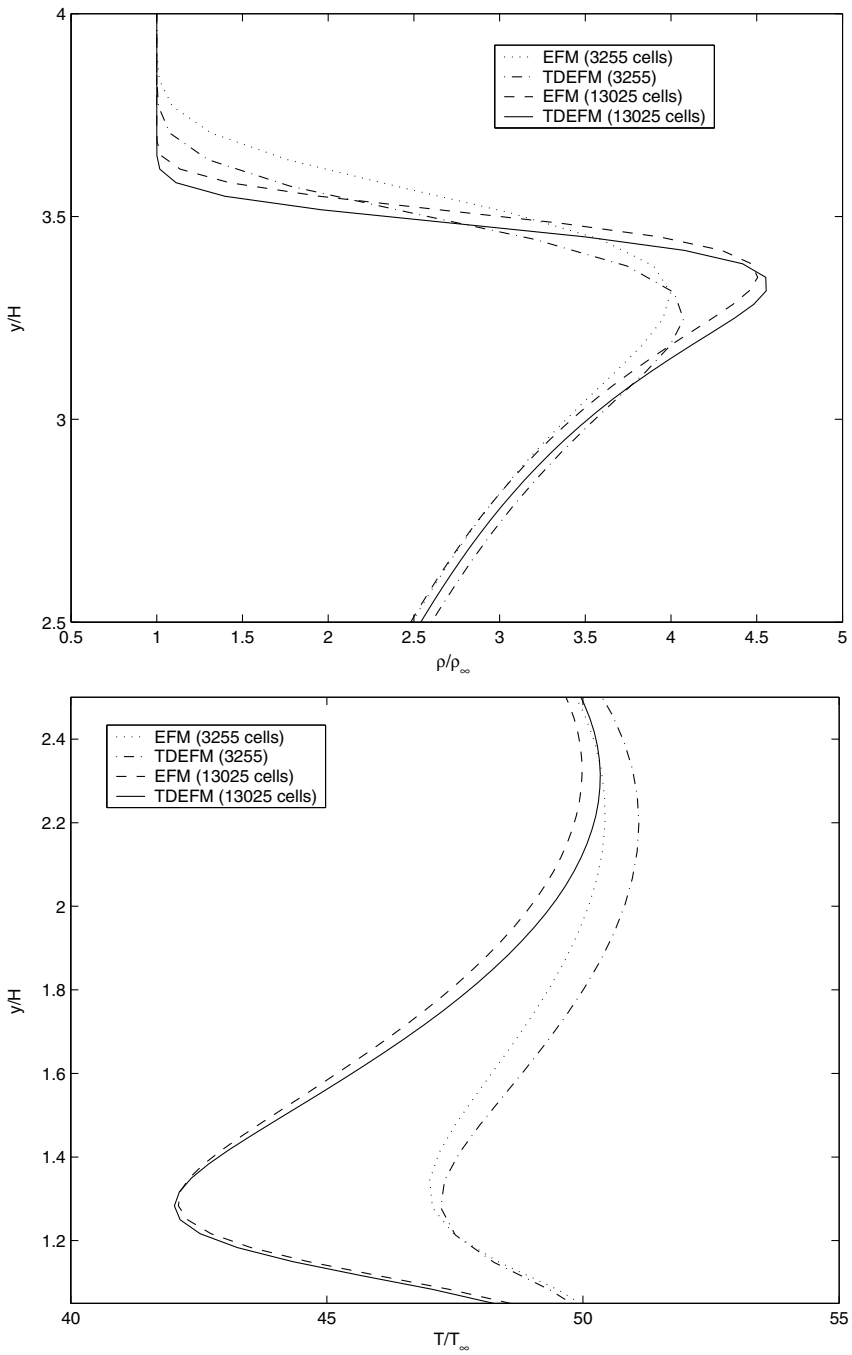

Fig. 16. Density profiles (top) and temperature profiles (bottom) from EFM and TDEFM solutions using various mesh densities. The results shown are alone line A-A' as shown in Fig. 14. The temperature profile is in the region ($1 \geqslant y/H \geqslant 2.5$). The density profile is in the region ($2.5 \geqslant y/H \geqslant 4$). Flow is at Mach 20 with $\gamma = 1.4$. Initial conditions are $\rho = \rho_\infty, M = M_\infty$ and $T = T_\infty$. The simulations are progressed in time to $t\sqrt{RT_\infty}/H = 3$.

Table 1
Shock standoff distances for varying computational grids

Method	Number of cells	Standoff distance Δ/H	Relative shock Standoff distance
TDEFM	3255	1.118	1
EFM	3255	1.185	1.06
EFM	3596	1.163	1.04
TDEFM	13,050	1.0195	1
EFM	13,050	1.05	1.03

where the flow is closer to the body and better aligned with the computational grid. The results demonstrate that the difference between the methods decreases where the flow is better aligned with the grid. As the flow direction diverges from grid alignment, i.e. as the distance y/H increases along line A–A′, the difference between the results is shown to increase.

As may be expected, the shock stand off distance is also affected. Presented in Table 1 are the shock standoff distances using TDEFM and EFM with varying mesh densities. The shock standoff distance is defined here as the location along $y = 0$ where the mach number equals unity. Since TDEFM (in its simplified form) is typically 10% computationally slower than EFM, tests were performed using EFM with a correspondingly larger number of cells. While the results improve slightly, the difference between the results is still significant. In terms of the shock standoff distance, increasing the number of cells from 3522 to 3596 decreased the difference in normalised shock standoff distance from 6% to 4%. Similar trends were shown with increasing mesh densities. Therefore, we conclude that the benefits of direction coupling outweigh the slight increase in computational expense.

8. Conclusion

Direction decoupling is defined here as the procedure used by finite volume solvers in CFD where 2D flow problems are solved by a series of one-dimensional fluxes, calculated by finding normal components to a cell interface. These fluxes are only exchanged between cells sharing a common interface, ignoring other physically realistic flows to adjacent cells not sharing an interface.

In order to show the effects of direction decoupling, the implementation of TDEFM on a structured, uniform rectangular mesh has been investigated and compared to the direction decoupled equilibrium flux method (EFM). These two methods are identical for small time steps and differ only in the fact that TDEFM is direction coupled while EFM is not. The methods were compared by simulating a blast wave problem and an implosion problem, for which the solution is expected to be radially symmetric. All simulations have been restricted to first order in space and time. The deviation of the solutions from axisymmetry is an indication of the errors associated with the different flux methods. This deviation was quantified by the angle between the radial position vector and the flow velocity vector for any point in the flow.

Results show that on a structured, uniform rectangular mesh TDEFM captures flows with significantly greater accuracy, as measured by flow symmetry, than the comparable direction decoupled method on the same mesh. TDEFM was then applied to a steady hypersonic flow problem, showing that the detached bow shock was moved further away from the body as a direct result of direction decoupling. The steady flow problem also demonstrated that the effects of direction decoupling do not disappear in the steady flow limit. We conclude that the direction decoupling of the fluxes in 2D flows can have significant detrimental effects in the accuracy of the solutions.

Acknowledgements

We gratefully acknowledge the contributions of M.N. Metchnik and P.A. Pinto of the Steward Observatory, University of Arizona for their input into the development of the TDEFM flux expressions.

Appendix A. TDEFM Flux expression coefficients

Mass coefficients

$$M_c = \frac{s\Delta t}{(x_R - x_L)\sqrt{2\pi}},$$

$$M_1 = \frac{1}{2(x_R - x_L)}(m\Delta t - x_l + x_R),$$

$$M_2 = \frac{1}{2(x_R - x_L)}(m\Delta t - x_r + x_R),$$

$$M_3 = \frac{1}{2(x_R - x_L)}(m\Delta t - x_l + x_L),$$

$$M_4 = \frac{1}{2(x_R - x_L)}(m\Delta t - x_r + x_L).$$

Momentum coefficients

$$P_c = \frac{ms\Delta t}{(x_R - x_L)\sqrt{2\pi}},$$

$$P_1 = \frac{1}{2(x_R - x_L)}(m(m\Delta t - x_l + x_R) + s^2\Delta t),$$

$$P_2 = \frac{1}{2(x_R - x_L)}(m(m\Delta t - x_r + x_R) + s^2\Delta t),$$

$$P_3 = \frac{1}{2(x_R - x_L)}(m(m\Delta t - x_l + x_L) + s^2\Delta t),$$

$$P_4 = \frac{1}{2(x_R - x_L)}(m(m\Delta t - x_r + x_L) + s^2\Delta t).$$

Energy coefficients

$$E_c = \frac{(2C + m^2 + 2s^2)s\Delta t}{2(x_R - x_L)\sqrt{2\pi}},$$

$$E_1 = \frac{1}{4(x_R - x_L)}\left((m^2 + s^2 + 2C)(m\Delta t - x_l + x_R) + 2ms^2\Delta t\right),$$

$$E_2 = \frac{1}{4(x_R - x_L)}\left((m^2 + s^2 + 2C)(m\Delta t - x_r + x_R) + 2ms^2\Delta t\right),$$

$$E_3 = \frac{1}{4(x_R - x_L)}\left((m^2 + s^2 + 2C)(m\Delta t - x_l + x_L) + 2ms^2\Delta t\right),$$

$$E_4 = \frac{1}{4(x_R - x_L)}\left((m^2 + s^2 + 2C)(m\Delta t - x_r + x_L) + 2ms^2\Delta t\right).$$

References

[1] D.I. Pullin, Direct simulation methods for compressible ideal gas flow, J. Comput. Phys. 34 (1980) 231–244.
[2] P.A. Jacobs, MBCNS: a computer program for the simulation of transient compressible flows, 1998 Update, Department of Mechanical Engineering Report 7/98, The University of Queensland, June 1998.
[3] M.N. Macrossan, M.R. Smith, M. Metchnik, P.A. Pinto, True direction equilibrium flux method: applications on rectangular 2D meshes', in: The Proceedings of 25th International Symposium on Rarefied Gas Dynamics, 21–28th July, 2006, St. Petersburg, Russia.
[4] M.R. Smith, M.N. Macrossan, M.M. Abdel-jawad, A. Ferguson, DSMC in the Euler limit and its approximate kinetic theory fluxes, In Proceedings of the 14th National Taiwan CFD Conference, 16–18th August, 2007, Nantou, Taiwan.

[5] G.A. Bird, Molecular Gas Dynamics and the Direct Simulation of Gas Flows, Clarendon Press, Oxford, 1994.
[6] L.N. Long, A. Sharma, Numerical simulation of the blast impact problem using the direct simulation Monte Carlo (DSMC) method, Journal of Computational Physics 200 (2004) 211–237.
[7] C.L. Merkle, H.W. Behrens, R.D. Hughes, Application of the Monte-Carlo simulation procedure in the near continuum regime' in rarefied gas dynamics, in: S.S. Fisher (Ed.), Prog. Astro. Aero., vol. 74, AIAA, New York, 1981, pp. 256–268.
[8] J.C. Lengrand, M. Raffin, J. Allegre, Monte Carlo simulation method applied to jet wall interactions under continuum flow conditions, in: S.S Fisher (Ed.) Rarefied Gas Dynamics, Prog. Astro. Aero., vol. 74, AIAA, New York, 1981, pp. 994–1006.
[9] G. Cook, High Accuracy Capture of Curved Shock Fronts Using the Method of Space–Time Conservation Element and Solution Element, AIAA Technical Paper 3277, AIAA Press, Washington, DC, 1999.
[10] M.N. Macrossan, 'The equilibrium flux method for the calculation of flows with non-equilibrium chemical reactions', J. Comput. Phys. 80 (1989) 204–231.
[11] M.N. Macrossan, D.I. Pullin, A computational investigation of inviscid hypervelocity flow of a dissociating gas past a cone at incidence, J. Fluid Mech. 266 (1994) 69–92.
[12] M.N. Macrossan, Hypervelocity flow of dissociating nitrogen downstream of a blunt nose, J. Fluid Mech. 207 (1990) 167–202.
[13] E.R. Mallett, D.I. Pullin, M.N. Macrossan, Numerical study of hypersonic leeward flow over a blunt nosed delta wing, AIAA J. 33 (1995) 1626–1633.
[14] B. Van Leer, Flux-vector splitting for the Euler equations, Lect. Notes Phys. 170 (1982) 507–512.
[15] M.N. Macrossan, M. Metchnik, P.A. Pinto, Hypersonic flow over a wedge with a particle flux method, in: Capetilli, Mario (Eds.), 24th International Symposium on Rarefied Gas Dynamics, vol. 762, 10–16th July, 2004, pp. 650–656.